International Journal of Hydrogen Energy 64 (2024) 896–905

Contents lists available at ScienceDirect

International Journal of Hydrogen Energy

journal homepage: www.elsevier.com/locate/he

Molecular dynamics insights into gas-water interfacial tension: Optimizing hydrogen storage in subsurface conditions

Qiuhao Chang [a], David Dempsey [a,**], Liehui Zhang [b], Yulong Zhao [b], Liangliang Huang [c,*]

[a] Department of Civil and Natural Resources Engineering, University of Canterbury, New Zealand
[b] National Key Laboratory of Oil and Gas Reservoir Geology and Exploitation, Southwest Petroleum University, China
[c] School of Sustainable Chemical, Biological and Materials Engineering, University of Oklahoma, United States

A B S T R A C T

This study presents a comprehensive analysis of interfacial tension (IFT) between pore water and hydrogen-cushion gas mixtures in subsurface porous media, a key variable in the distribution of gas mixtures for hydrogen storage. Employing molecular dynamics simulations, we developed two IFT models at 20 MPa and 373 K: one for an H_2–CO_2–H_2O system and another for an H_2–CH_4–H_2O system. The models reveal that increasing cushion gas concentration reduces gas-water IFT. Notably, for H_2–CO_2–H_2O mixtures, the IFT substantially decreases with CO_2 concentration up to 40%, after which the reduction rate diminishes. In H_2–CH_4–H_2O mixtures, the IFT decreases linearly with CH_4 concentration. The study attributes these variations to local density distributions and molecular orientation effects. Specifically, CO_2 adsorption at the interface up to 40% concentration significantly lowers IFT, while CH_4 adsorption proportionally decreases IFT. The influence of CO_2 on water molecule orientation at the interface, in contrast to the non-effect of CH_4, is also critical in enhancing IFT reduction. Our results also highlight the reduction of H_2 self-diffusion at the interface caused by CO_2 and CH_4, an essential factor in optimizing subsurface hydrogen storage operations.

1. Introduction

Hydrogen has long been recognized as a cornerstone for the transition to a sustainable energy landscape. From its nascent inclusion in the energy dialogue to its pivotal role in achieving global net-zero emission targets, hydrogen's versatility is undisputed in its application across transportation, industrial processes, and electricity generation sectors [1–3]. Its versatility is evident in applications from transportation fuel to electricity generation, with its production exceeding 90 million metric tons in 2020 and projected to increase annually [4,5]. The Hydrogen Council estimates that achieving net-zero will require around 660 million tons of hydrogen by 2050, equating to 22% of forecasted global energy demand [6]. The surface storage technologies such as physical storage through compression, liquefaction, and adsorption or chemical storage through metal hydrides and fuel cells may eventually be unable to meet such large hydrogen demand [7–10]. On the other side, given the experimental nature of conventional storage methods, the vast capacity of underground porous media like aquifers and depleted hydrocarbon reservoirs has proven essential for large-scale hydrogen storage, as demonstrated by successful global implementations [11–14]. The operational cornerstone of subsurface hydrogen storage lies in the injection of a cushion gas—commonly CO_2 or CH_4—to form a compressible gas plume, enabling cyclical storage modulation through pressure dynamics [11,15–20]. A critical determinant in this process is the interfacial tension (IFT) between the hydrogen-cushion gas mixture and in-situ water. IFT dictates the displacement efficiency of water and the distribution of the gas within the porous media, influencing the overall storage efficacy [21–26].

While historical research on IFT has been primarily centered on hydrogen-water interactions, recent investigations have illuminated the intricate effects of temperature, pressure, and salinity on these interactions. For instance, studies by Slowinski et al., and Massoudi and King reported minimal pressure effects on the IFT at standard temperatures [27,28], while Chow et al., observed a pronounced temperature dependency within an extensive pressure range [29]. Similarly, Al-Mukainah et al., and Hosseini et al., correlated IFT increases directly with salinity across diverse temperature and pressure conditions [30,31]. The recent body of work delves into the IFT dynamics of hydrogen when combined with cushion gases. It has been established that CO_2 integration reduces the IFT, with the most notable effects under increased temperatures and pressures, though diminishing above 20 MPa [29,32]. Investigations by Zoha et al., Doan et al., and Mirchi et al., extended these findings, linking CO_2 concentration and CH_4 presence with reduced IFT, particularly under varying temperature conditions

* Corresponding author.
** Corresponding author.
E-mail addresses: david.dempsey@canterbury.ac.nz (D. Dempsey), HLL@ou.edu (L. Huang).

https://doi.org/10.1016/j.ijhydene.2024.03.341
Received 22 January 2024; Received in revised form 6 March 2024; Accepted 27 March 2024
Available online 3 April 2024

[21,33–35].

Yet, the current scientific understanding remains limited, especially concerning the effects of fluctuating gas concentrations over time—a critical aspect affecting the relative permeability in multi-component flow and, hence, the spatial distribution of gas and water in underground storage porous media [36–41]. Traditional laboratory approaches have been unable to decipher the nanoscale mechanisms that drive IFT changes. This study, therefore, focuses on an analysis of the IFTs between water and H_2–CO_2, and H_2–CH_4 mixtures across the full concentration range, and under typical subsurface storage conditions (20 MPa, 373 K) [42,43]. Using molecular dynamics (MD) simulations, we explore the molecular behaviors at the gas-water interface, focusing on adsorption, orientation, and diffusion. Our insights contribute to a refined understanding of IFT evolution, which will contribute to more efficient and secure hydrogen storage. The manuscript is structured sequentially: Section 2 defines the gas-water models and simulation details; Section 3 describes the findings on gas-water IFT and molecular interactions; Section 4 proposes avenues for future research; and Section 5 presents our conclusions.

2. Models and simulation details

We used the Large-scale Atomic/Molecular Massively Parallel Simulator (LAMMPS) for MD simulations to quantify the interfacial properties of two distinct systems at 20 MPa and 373 K: (a) binary gas-water systems, specifically H_2/H_2O, CO_2/H_2O, and CH_4/H_2O; and (b) ternary systems comprising H_2/CO_2 and H_2/CH_4 gas mixtures with water. This methodology builds upon our previously established approach for investigating interfacial phenomena between immiscible phases [44].

For the binary systems, we initiated the simulations by positioning 3000 water molecules centrally, flanked by 1000 gas molecules of either H_2, CO_2, or CH_4 on each side, creating a system of 5000 molecules within a simulation box measuring 5 nm by 5 nm by 30 nm. For each system, the 1-ns equilibration in the canonical ensemble (NVT) was firstly performed to mitigate molecular overlap, followed by another 15-ns calculation in the isothermal–isobaric ensemble (NPT) to further equilibrate the system. Then, a production run of 10 ns was performed, with the last 2-ns trajectory collected for the property analysis. Each simulation model was repeated four times for each concentration case to ensure the robustness and reproducibility of our results. The ternary systems followed a similar setup, with 3000 water molecules at the core and varying ratios of cushion gas to H_2 on either side. We explored six different molar ratios for CO_2 and CH_4 with H_2, ranging from 10% to 80% cushion gas concentration. A table of the number of gas molecules in each system was listed in the supporting materials (Table S1). The simulation protocols for the ternary systems mirrored those of the binary systems, including ensemble application and data collection phases. We note that for reporting bulk vapor pressure in our simulations, we reported the pressure as the average of $(P_{xx} + P_{yy} + P_{zz})/3$. The use of the NPT ensemble is supported by its successful application in similar interfacial studies [45–48]. These studies demonstrated the NPT ensemble's ability to equilibrate vapor-liquid and liquid-liquid systems, justifying its selection for our work on gas-water interfaces. However, if the system involves a solid substrate, for example, the liquid/solid system, reporting the P_{zz} value and utilizing the $NP_{zz}T$ ensemble would be better, as the P_{zz} component accurately represents the tension along the interface normal [49–51].

Force field models—EPM2 for CO_2 [52,53], TIP3P for water [54,55], TraPPE-UA for CH_4 [56], and the Vrabec single-site model for H_2 [57]—were selected based on their demonstrated reliability in simulating interfacial interactions involving these species [44,58–61]. The suitability of TIP3P for these systems is well-established in literature, including the works of Vega and de Miguel [62], and Chen and Smith [63], who have previously reported the surface tensions using the TIP3P model. Our choice of the TIP3P water model is further supported by its adequacy in describing vapor-liquid equilibria (VLE) of H_2O–H_2 mixtures as demonstrated by Rahbari et al. [64], and its accuracy for predicting IFT in CH_4-water and CO_2-water systems at high pressures, as shown by Chen et al. [55] However, interfacial property studies with other water models, such as TIP4P/2005(*59*), have been reported.

Throughout the MD simulations, we applied periodic boundary conditions across all three dimensions for binary and ternary systems. The leapfrog integrator was utilized with a time step of 1 fs. Electrostatic interactions were computed using the particle-particle-particle mesh (PPPM) method, and the non-bonded van der Waals forces were described by the 12-6 Lennard-Jones potential. A cutoff radius of 15 Å was applied for LJ interactions. A cutoff of 15 Å was applied for Coulombic interactions, beyond which the PPPM method, with the accuracy of 1.0e-5, was used to handle long-range electrostatic interactions. The LJ interatomic potential parameters between species were calculated using the Lorentz-Berthelot mixing rules. Temperature and pressure were controlled using the Nose-Hoover thermostat and barostat during the simulations within the NVT and NPT ensembles, respectively. Fig. 1**(a)**, **1(b)**, and **1(c)** depict the equilibrium states of the binary and ternary systems, respectively, as obtained from the MD simulations.

3. Results and discussions

3.1. Interfacial tension

The interfacial tension between the gas and water was determined through the Gibbs IFT formulation [65]:

$$r = -\frac{1}{2}\left(\frac{P_{xx} + P_{yy}}{2} - P_{zz}\right)L_z$$

where L_z is the length of the simulation box along the z-direction. P_{xx}, P_{yy}, and P_{zz} are three diagonal elements of the pressure tensor. The coefficient ½ represents the two interfaces existing. Fig. 1 shows the existence of two interfaces, perpendicular to the z-direction.

The calculated interfacial tensions (IFTs) for binary H_2–H_2O, CH_4–H_2O, and CO_2– H_2O systems at 20 MPa and 373 K were 55 mN/m, 42 mN/m, and 31 mN/m, respectively. These values exhibit strong concordance with reference data reporting IFTs of 58 mN/m for H_2-water [29], 44 mN/m for CH_4-water [66], and 29 mN/m for CO_2-water [67], as detailed in Table 1. Despite the underestimate for the CH_4/H_2O system, those general agreements corroborate the reliability of our MD simulations. In addition, the densities of CH_4, CO_2, H_2, and H_2O were calculated separately and compared with the NIST database at 373 K and 20 MPa in the supporting material (Table S2) for the validation of the force fields.

In Fig. 2(a), we present the quantified interfacial tension (IFT) at the gas-water interface as a function of CO_2 and CH_4 concentrations in their respective ternary systems with H_2 under 20 MPa and 373 K conditions. The data illustrate a trend where an increase in the proportion of cushion gas in the mixture with H_2 corresponds to a decrease in the IFT. This finding generally aligns with the observations of Chow et al. [29] for the CO_2–H_2–H_2O system and with the results obtained by Zoha et al. [21] and Doan et al. [33] for their respective CO_2–H_2–H_2O and CH_4–H_2–H_2O systems. However, direct quantitative comparisons with existing literature are challenging due to the scarcity of data under identical conditions. For instance, Chow et al.'s study was limited to a 0.3 CO_2 concentration, whereas Zoha et al. conducted their research at different temperatures. Nevertheless, the CO_2–H_2 gas mixture exhibits a lower IFT than the CH_4–H_2 mixture at equivalent concentrations of cushion gas. Furthermore, as depicted in Fig. 2(b), a significant observation within the CO_2–H_2–H_2O system is that the IFT decreases substantially as the CO_2 concentration increases from 0% to 40%, after which the rate of decrease moderates from 40% to 100% CO_2. In contrast, the IFT in the CH_4–H_2–H_2O system diminishes linearly with

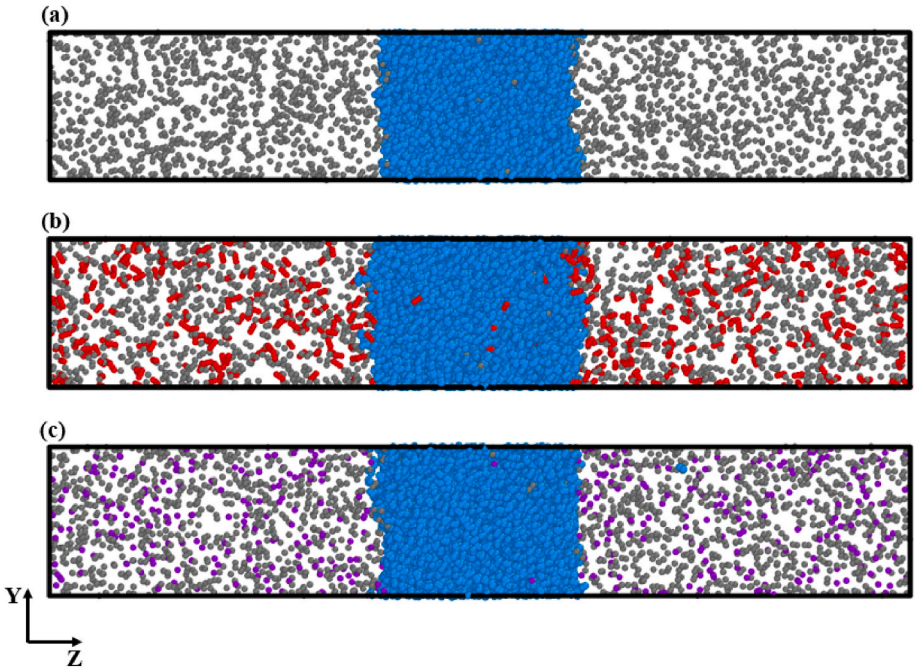

Fig. 1. The equilibrium state of binary and ternary systems at 20 MPa and 373 K. (a). Binary system of hydrogen and water, grey: H_2, blue: H_2O. (b). Ternary system of (CO_2+H_2)/H_2O, red: CO_2. (c). Ternary system of (CH_4+H_2)/H_2O, purple: CH_4. (For interpretation of the references to colour in this figure legend, the reader is referred to the Web version of this article.)

Table 1
The IFT of three binary systems from this work and previous publications.

Gas-Water	IFT-MD (mN/m)	IFT-Ref (mN/m)	Error%
H_2-Water	57	53-58([29,58,68])	1.7–7.5
CH_4-Water	42	44-49([66,69,70])	4.5–14.3
CO_2-Water	31	29-32([67,71,72])	3.1–6.9

increasing CH_4 concentration.

3.2. Local density profile

In analyzing phase separation within the simulated H_2–H_2O system, local density profiles serve as a critical metric for delineating the bulk and interfacial regions. Fig. 3 illustrates the calculated local densities of H_2 and H_2O molecules along the z-axis. Given the negligible solubility of H_2 in water, a distinct separation between the gas and liquid phases is observed. In the H_2-dominated phase (region I), the water density profile is near zero, signifying a gas-rich environment. Conversely, in the water-dominated phase (region III), the H_2 density profile tends toward zero, indicating a liquid-rich region. The interface between these phases (region II) is identified by the points where the density profiles of water and hydrogen fall to zero, marking the boundaries of the interfacial region. The local density profiles of CO_2-Water and CH_4-Water systems were determined and plotted in Fig. S1 of the supporting materials. In addition, the solubilities of gases in the water were determined based on their densities in the water and compared with reference values in Table S3 of the supporting materials for further validation.

In the studied ternary systems, such as the (30% CO_2 + 70% H_2)/H_2O and (30% CH_4 + 70% H_2)/H_2O configurations depicted in Fig. 4, the local density profiles for CO_2 and CH_4, alongside H_2O and H_2, were analyzed. The profiles reveal a significant decline in the local densities of

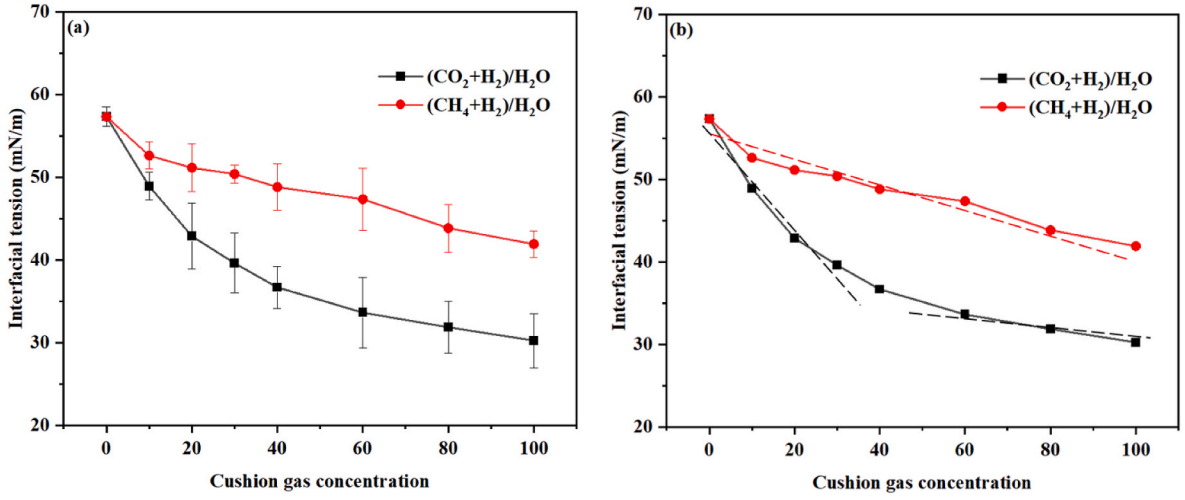

Fig. 2. (a) IFTs of (CO_2+H_2)/H_2O and (CH_4+H_2)/H_2O systems at 20 MPa and 373 K with different cushion gas concentrations. (b) The IFT curves fittings.

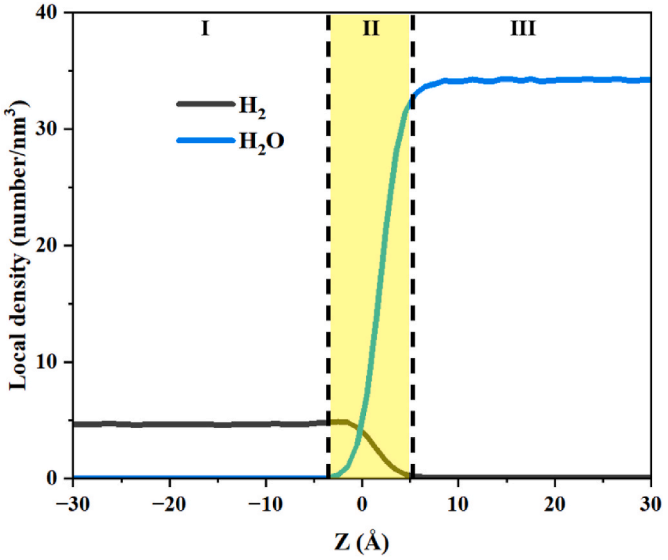

Fig. 3. The local density profiles of the H_2-water system at 373K and 20 MPa.

CO_2 and CH_4 within the water-rich phase, corroborating their limited solubility in water. Distinct from H_2, the local densities of CO_2 and CH_4 are elevated in the interfacial region compared to the gas-rich phase. This indicates their preferential adsorption and accumulation at the gas-water interface—a phenomenon previously documented in the literature [73–75].

Notably, the interface region's local density of CO_2 exceeds that of CH_4 at an equivalent 30% concentration, suggesting a superior adsorption propensity of CO_2 molecules. This differential adsorption is attributed to the molecular interactions between the gas molecules and water at the interface. Quantitative analysis of the interaction energies reveals that CO_2–H_2O interactions (−537 kcal/mol) are substantially stronger than CH_4–H_2O interactions (−122 kcal/mol). Consequently, CO_2 exhibits a more pronounced adsorption at the gas-water interface than CH_4, as reflected by the higher interaction energy values.

In Fig. 5, we present the local density profiles of CO_2 and CH_4 across different concentrations, while Fig. 6 outlines the corresponding profiles for H_2. The local densities of the cushion gases in both the gas-rich phase and the interface region exhibit an increase correlating with rising cushion gas concentrations. At the studied conditions of 20 MPa and 373 K, CO_2 exists in a supercritical state, unlike CH_4, which remains gaseous [76]. This distinction results in a higher local density for supercritical CO_2 than for gaseous CH_4 within the gas-rich phase at equivalent concentrations. Additionally, CO_2's more robust adsorption capacity than CH_4 leads to its greater local density at the gas-water interface for each concentration.

Furthermore, Fig. 6 indicates a decrease in H_2 local densities within the gas-rich and interface regions with increasing cushion gas concentration. This trend suggests that increased cushion gas adsorption at the interface diminishes the direct interaction between H_2 and H_2O molecules—consequently, the gas-water IFT transition from being predominantly influenced by H_2 to being governed by cushion gases.

As shown in Fig. 7, the right-side interface region of the (CO_2+H_2)/H_2O system is depicted for various CO_2 concentrations, illustrating the adsorption behavior at the molecular level as obtained from the MD simulation. The visualization reveals a higher accumulation of CO_2 molecules within the interface region compared to the gas-rich phase, particularly pronounced at 20% and 40% CO_2 concentrations. This observation aligns with the local density profiles presented in Fig. 4(a). Furthermore, a positive correlation is noted between the CO_2 concentration and its accumulation at the interface region, corroborating the data in Fig. 5(a). This trend underscores the concentration-dependent nature of CO_2 interfacial adsorption behavior in the studied system.

3.3. Incremental adsorption mechanism

As discussed in Section 3.2, we observed an increase in cushion gas densities within the gas-rich phase and at the interface as the gas concentration in the system was raised. To elucidate the adsorption mechanisms at the gas-water interface, we evaluated the relative density profiles of the cushion gases at varying concentrations. Here, the relative density (ρ_r) of a cushion gas is defined as the ratio of its local density at the interface (ρ_{local}) to its bulk density in the gas-rich phase (ρ_{bulk}):

$$\rho_r = \frac{\rho_{local}}{\rho_{bulk}}$$

Fig. 8(a) and **8(b)** display the relative density profiles for CO_2 and CH_4, respectively. In the (CO_2+H_2)/H_2O system, relative densities of CO_2 remain approximately constant at 2 for concentrations ranging from 10% to 40%. This constancy suggests a proportional relationship between the adsorbed CO_2 at the interface and the CO_2 in the gas-rich phase at concentrations below 40%. However, beyond a 40% CO_2 concentration, relative densities at the interface decrease with increasing concentration, indicating a saturation effect where further adsorption of CO_2 becomes increasingly difficult.

Conversely, in the (CH_4+H_2)/H_2O system, the relative densities of CH_4 at the interface maintain a steady proportionality to the densities in

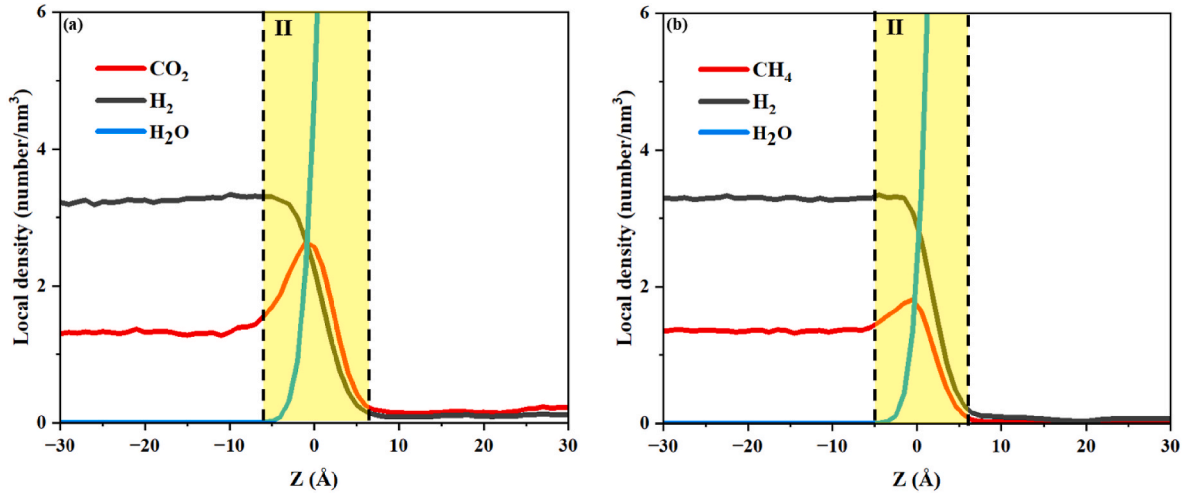

Fig. 4. The local density profiles: (a) (CO_2+H_2)/H_2O system with 30% CO_2 concentration. (b) (CH_4+H_2)/H_2O system with 30% CH_4 concentration.

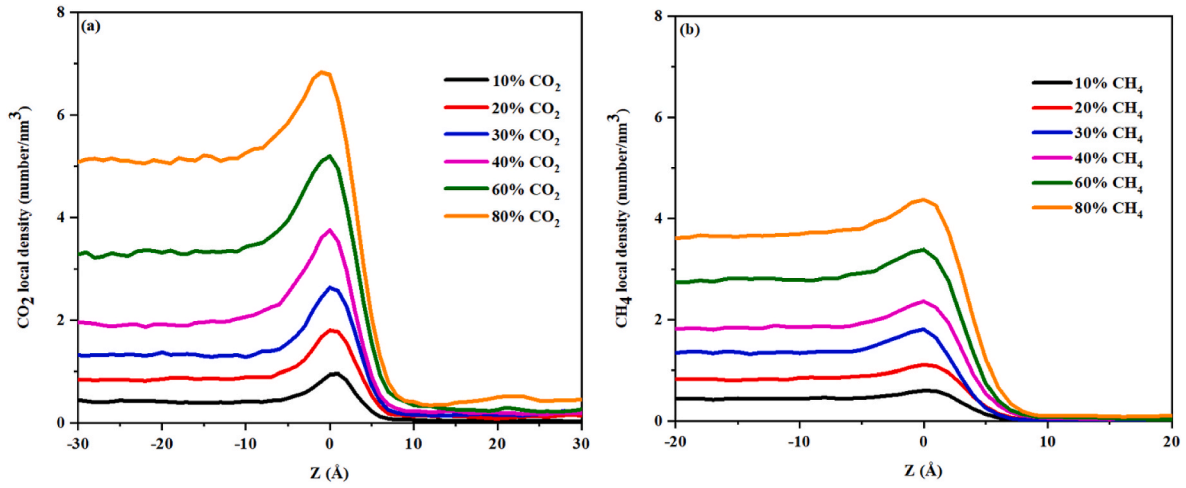

Fig. 5. The local density profiles: (a) CO_2 in $(CO_2+H_2)/H_2O$ system with different CO_2 concentrations. (b) CH_4 in $(CH_4+H_2)/H_2O$ system with different CH_4 concentrations.

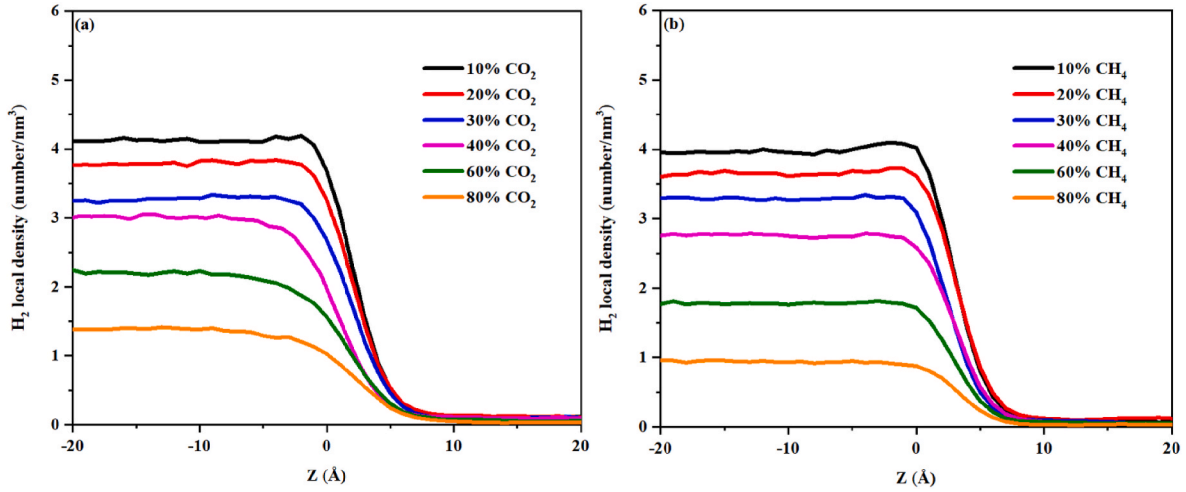

Fig. 6. The local density profiles: (a) H_2 in $(CO_2+H_2)/H_2O$ system with different CO_2 concentrations. (b) H_2 in $(CH_4+H_2)/H_2O$ system with different CH_4 concentrations.

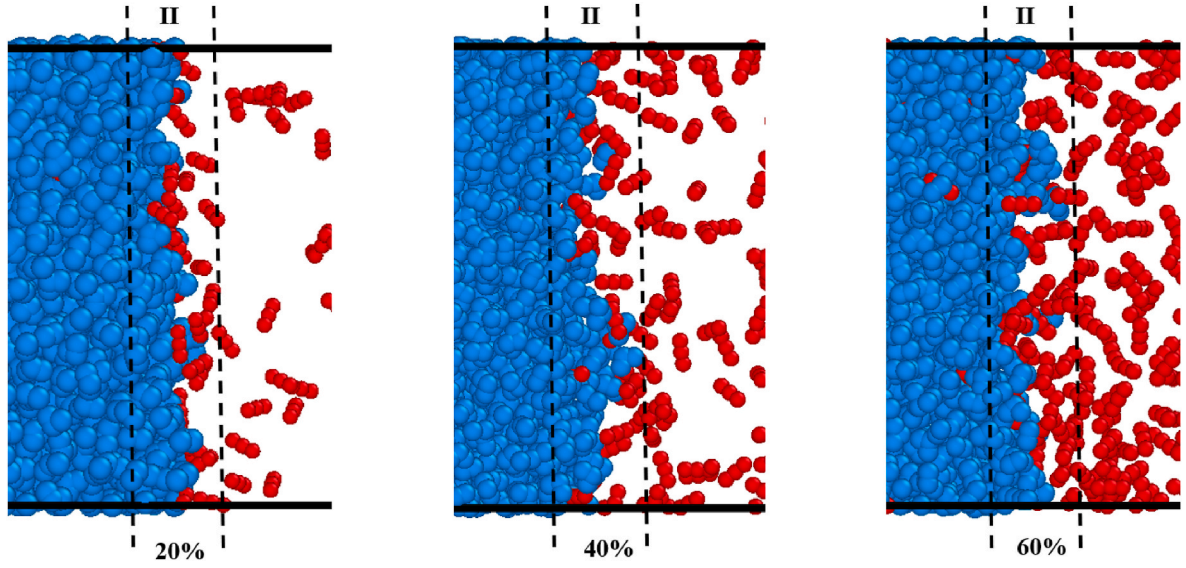

Fig. 7. Visualization of CO_2 molecules near the gas-water interface region with different concentrations. H_2 molecules on the right are not shown for clarity.

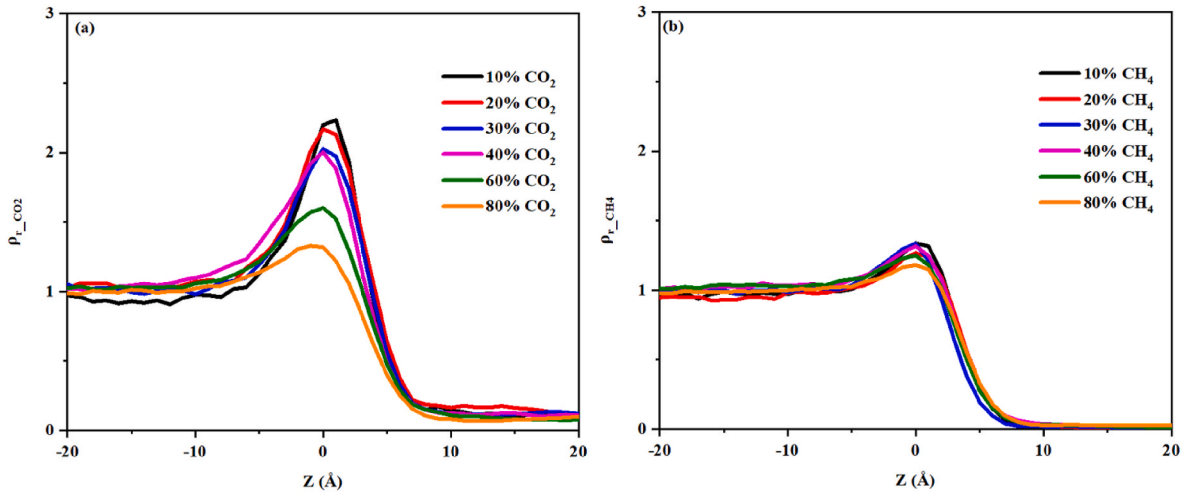

Fig. 8. Relative density profiles at different concentrations: (a) CO_2; (b) CH_4.

the gas-rich phase, irrespective of concentration. This behavior aligns with the IFT findings: in the $(CO_2+H_2)/H_2O$system, CO_2 molecules are readily adsorbed at the interface at lower concentrations (0–40%), leading to substantial reductions in IFT. Once the interface region becomes saturated with CO_2 at around 40% concentration, additional CO_2 adsorption becomes more challenging, resulting in minor IFT variations. Meanwhile, in the $(CH_4+H_2)/H_2O$ system, a consistent decrease in IFT is observed as the CH_4 concentration increases, attributed to the continuous adsorption of CH_4 at the interface.

3.4. Molecular orientation

The influence of molecular orientation on interfacial tension is well-documented at the molecular level [44,77]. We investigated the orientation of cushion gas and water molecules at the gas-water interface by calculating the orientational order parameter (S). This parameter quantifies the preferential alignment of molecules relative to the interface as a function of their z-directional positioning [78]:

$$S = \frac{1}{2} < 3\ cos^2(\theta) - 1 >$$

Here, θ represents the angle between the CO_2 molecule's centerline, the water molecule's dipole vector, and the z-axis. For CO_2, the preferential parallel orientation to the interface corresponds to S values nearing −0.5, whereas S values near unity suggest a perpendicular orientation. Randomly oriented molecules would yield S values around zero.

The tetrahedral structure of CH_4 precludes a similar orientation analysis; hence, it was excluded from this portion of the study. Fig. 9 illustrates the orientational profiles for CO_2 and H_2O from the $(CO_2+H_2)/H_2O$ system with a 20% CO_2 concentration. The CO_2 local density profile aids in delineating the interface region. Within the gas-rich and water-rich phases, the S values for CO_2 and H_2O approximate zero, indicating random molecular orientation. In the interface region, CO_2 molecules exhibit an S value of about −0.05, indicating a slight preference for a parallel orientation to the interface. Water molecules present S values around −0.18 in the same region, suggesting a more pronounced preference for parallel alignment. These molecular orientations for CO_2 and water are consistent with previous findings in the literature [44,58,79,80].

To delve deeper into the orientation of CO_2 at the gas-water interface, Fig. 10 quantifies the S values for CO_2 across a range of concentrations. It is consistently observed that CO_2 molecules prefer alignment parallel to the interface at all studied concentrations. A notable trend is the positive increase in S values with rising CO_2 concentration, suggesting a diminished parallel orientation as the interface becomes

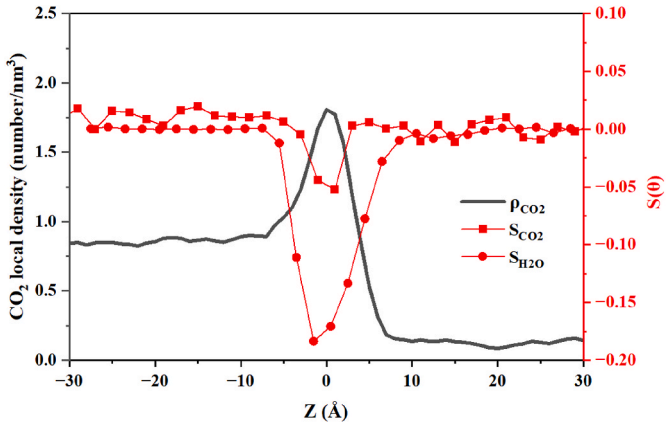

Fig. 9. Orientation profiles of CO_2 and H_2O molecules along the Z direction in the $(CO_2+H_2)/H_2O$ system with the 20% CO_2 concentration. The density profile (black) is used to emphasize the location of the gas-water interface region.

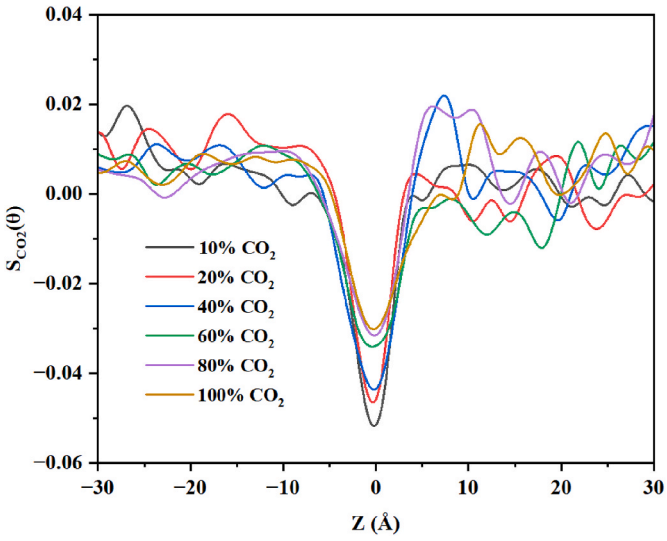

Fig. 10. CO_2 orientation profiles with different CO_2 concentrations.

increasingly populated with adsorbed CO_2 molecules. However, beyond a 40% concentration threshold, the S values plateau; for instance, CO_2 concentrations at 60%, 80%, and 100% maintain S values of approximately −0.03 within the interfacial region.

This behavior aligns with the previously discussed interfacial tension and relative density findings. At CO_2 concentrations exceeding 40%, additional free CO_2 molecules face challenges in adsorbing to the already crowded interface, thus resulting in minor variations in interfacial tension and the orientational behavior of CO_2 molecules.

Fig. 11(a) illustrates the orientational profiles of water molecules within (CO_2+H_2)/H_2O systems across varying CO_2 concentrations, while Fig. 11(b) presents the corresponding data for (CH_4+H_2)/H_2O systems with different CH_4 concentrations. In both ternary systems, water molecules exhibit a preferential orientation at the gas-water interface, aligning their dipole vectors parallel to the interface.

When cushion gas concentration is considered, water's orientational order parameter (S) remains consistently unchanged at the interface with increasing CH_4 concentrations. Conversely, the S values for water positively increase at the interface with rising CO_2 concentrations. This trend suggests that CO_2 adsorption at the gas-water interface modifies its interfacial orientation and significantly influences that of water molecules. In contrast, the interfacial orientation of water molecules remains unaffected by CH_4 adsorption. This differential impact on water molecule orientation by CO_2 compared to CH_4 could contribute to the observed discrepancy in gas-water IFT reductions between the (CH_4+H_2)/H_2O and (CO_2+H_2)/H_2O systems for the same concentration of cushion gas, as illustrated in Fig. 2.

3.5. Molecular diffusion

Subsurface microorganisms, such as methanogens and acetogens, predominantly thrive at the gas-water interface and their metabolic processes can involve the consumption of H_2, presenting a significant factor for consideration in UHS [81]. The self-diffusion of H_2 at the gas-water interface is relevant as it can affect microbial activity and, consequently, the consumption rate of H_2. This section investigates the impact of cushion gases on H_2 self-diffusion at the interface. Utilizing methodologies from Liu et al. [45] and Yuan et al. [82], we divided the binary and ternary systems along the Z-axis into five distinct slabs to calculate H_2 self-diffusion coefficients within each slab: two in the gas-rich phase, two at the interface, and one in the water-rich phase.

The mean-squared displacement (MSD) is used to quantify the self-diffusion coefficient of a gas, defined as [83,84]:

$$MSD(t) = < |r_i(t) - r_i(0)|^2 >$$

where $r_i(t)$ is the position of particle i at time t, $r_i(0)$ is the particle's initial position, and the brackets denote an ensemble average. The self-diffusion coefficient, D, is subsequently deduced from the MSD as:

$$D = \lim_{t\to\infty} \frac{1}{6t} MSD(t)$$

Self-diffusion coefficients in binary systems are initially evaluated, as indicated by the black line for H_2 in the H_2–H_2O system and the orange lines for CO_2 and CH_4 in the respective CO_2–H_2O and CH_4–H_2O systems depicted in Fig. 12. To validate these results, we referenced self-diffusion data for H_2 within calcite slit pores under comparable conditions of 20 MPa and 340 K [85]. Our simulation findings for the gas-rich phase are consistent with the reference values, exhibiting the same order of magnitude. In addition, Groß et al. [86] reported the experimental self-diffusion of CO_2 at 333 K and 20 MPa which was about 0.27×10^{-7} m^2/s. With the temperature effect studied in their paper, it is believed that the self-diffusion of CO_2 at 20 MPa and 373 K should be in the range between 0.3×10^{-7} m^2/s to 0.4×10^{-7} m^2/s, which is higher than our simulation result of 0.23×10^{-7} m^2/s in the bulk phase but very close to each other. The self-diffusion coefficient of bulk CH_4 reported from the experiment is around 1.4×10^{-7} m^2/s at 19 MPa and 353 K [87], compared with our simulation result of 0.6×10^{-7} m^2 at 20 MPa and 373 K, the difference exists but accepted in the order of magnitude. With the comparison of IFT shown in Table 1, the maximum IFT deviation of the CH_4-Water system could reach around 14.3%. We recommend a further refinement of the force field used for CH4 in such a vapor-liquid IFT system. Finally, since the solubilities of H_2 and CH_4 in the water are small (as shown in the SI materials), the experimental self-diffusions of H_2 and CH_4 in the water are scarce. However, a comparison was found related to CO_2 diffusion in the water under a similar P/T condition. The self-diffusion of CO_2 in the water from our simulation is around 8.6×10^{-9} m^2/s, consistent with the experimental result of approximately 7.45×10^{-9} m^2/s reported by Shane et al. [88].

Due to molecular weight differences, H_2 exhibits the highest self-diffusion, while CO_2 shows the lowest. In the gas-rich phase (region I), gas molecules demonstrate the highest self-diffusion coefficients, which diminish progressively towards and within the gas-water interface region (region II). Upon dissolution into the water-rich phase (region III), the self-diffusion coefficients of the gas molecules are notably reduced.

In ternary systems, the self-diffusion of H_2 diminishes in the presence of increasing concentrations of cushion gas. In the gas-rich phase, interactions between H_2 and cushion gas molecules lower H_2 self-diffusion due to the inherently lower self-diffusion of the cushion gases. The adsorption of cushion gas at the interface further impedes H_2 penetration, reducing its self-diffusion in this region. As cushion gas concentration escalates, the enhanced molecular interaction in the gas-rich

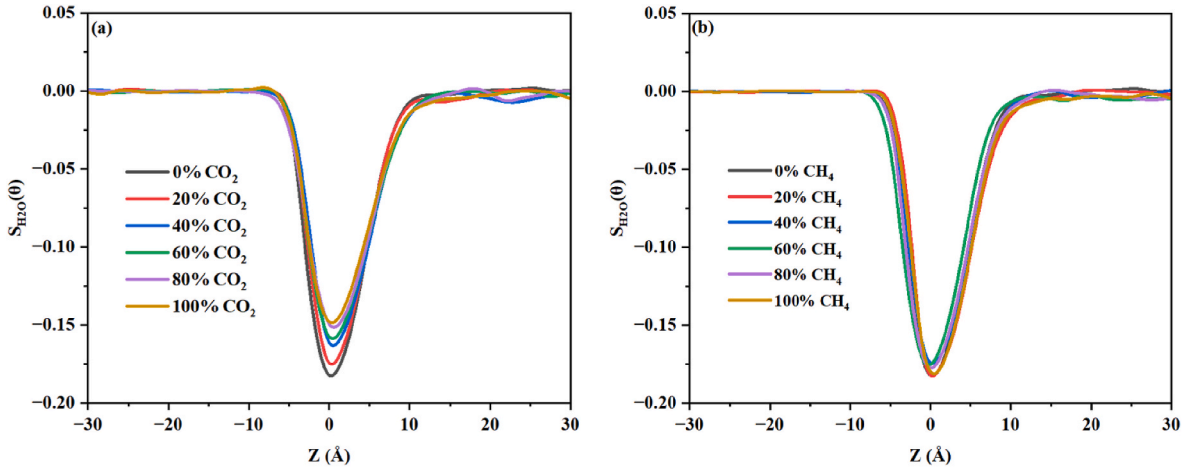

Fig. 11. H_2O orientation profiles from: (a) (CO_2+H_2)/H_2O system with different CO_2 concentrations. (b) (CH_4+H_2)/H_2O system with varying concentrations of CH4.

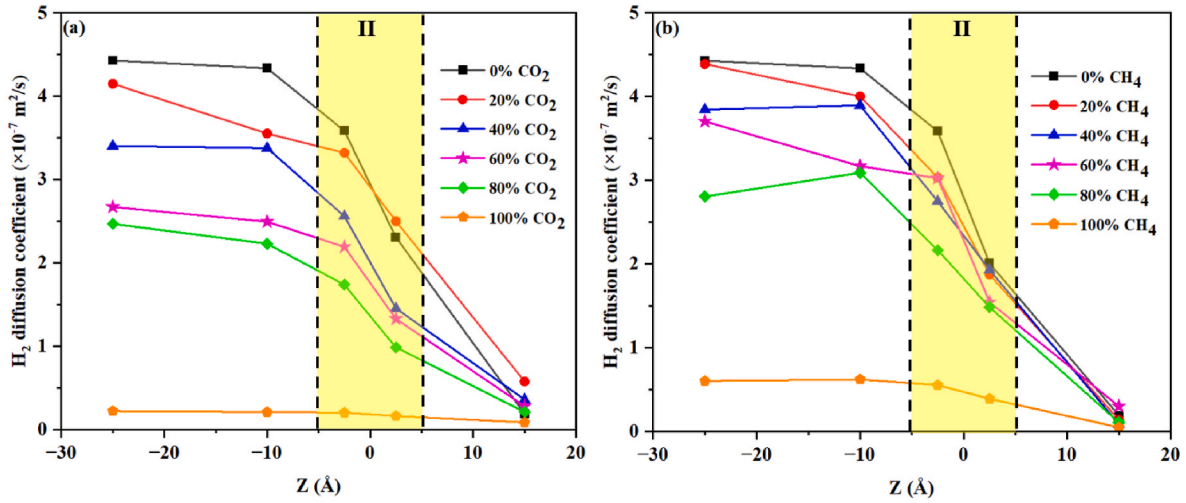

Fig. 12. H_2 self-diffusion coefficients in: (a) $(CO_2+H_2)/H_2O$ system with different CO_2 concentrations. (b) $(CH_4+H_2)/H_2O$ system with varying concentrations of CH4.

phase and the increasing accumulation of adsorbed cushion gas at the interface concomitantly decrease the self-diffusion of H_2, making it increasingly challenging for H_2 to diffuse through the interface region.

3.6. Further discussion

In this investigation, we have constructed two models to describe the IFT of gas-water systems at 20 MPa and 373 K, pertinent to UHS: one for $(CO_2+H_2)/H_2O$ mixtures and another for $(CH_4+H_2)/H_2O$ mixtures. It is acknowledged, however, that factors such as pressure and temperature also influence gas-water IFT, beyond gas concentration alone. Chow et al. [29], Pereira et al. [89], Liu et al. [90], and Kashefi et al. [70] have provided IFT measurements for H_2–H_2O, CO_2–H_2O, and CH_4–H_2O systems under varying pressures and temperatures, as detailed in Fig. 13. From their findings, we can infer that pressure notably impacts gas-water IFTs primarily at low-pressure regimes. Above the threshold of 20 MPa, IFT exhibits only marginal variations with further pressure increments, which suggests that the models developed herein can be applied across an extensive pressure range above 20 MPa at 373 K. In contrast, temperature has a pronounced effect on IFT; generally, an increase in temperature correlates with a decrease in gas-water IFT. For future work aimed at enhancing the comprehensiveness of IFT models for UHS, it is imperative to integrate the methodology from this study to quantify the (cushion gas + H_2)/H_2O IFT as a function of gas concentration, particularly at lower pressure ranges or across varying temperatures.

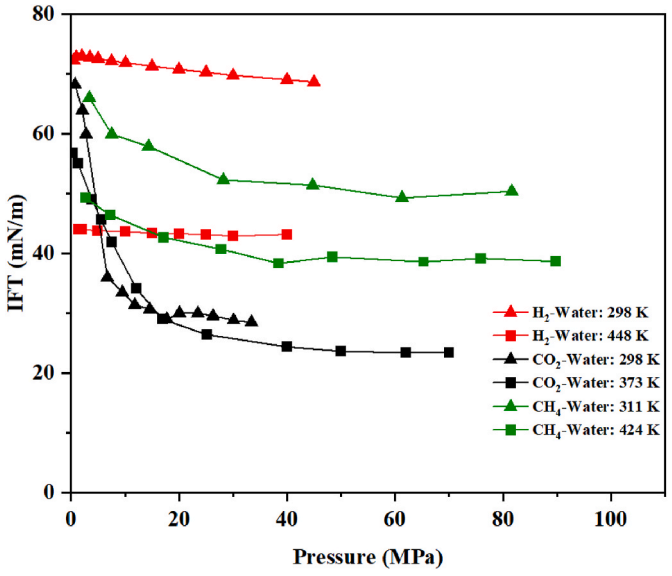

Fig. 13. The IFTs of H_2–H_2O, CO_2–H_2O, and CH_4–H_2O as a function of pressure and temperature reported from previous publications.

4. Conclusions

When evaluating subsurface porous media for hydrogen storage, the interfacial tension between pore water and a gas mixture of H_2 with a cushion gas is a critical factor influencing the displacement of residual water and the distribution of the gas mixture. Through molecular dynamics simulations, this study has formulated two models for gas-water IFT as a function of cushion gas concentration at the expected subsurface storage conditions of 20 MPa and 373 K: one for an H_2–CO_2–H_2O mixture and another for an H_2–CH_4–H_2O mixture. It has been consistently observed that an increase in the concentration of the cushion gas correlates with a reduction in gas-water IFT. A key finding is that for the H_2–CO_2–H_2O mixture, the IFT significantly decreases as CO_2 concentration increases up to 40%, beyond which the rate of decrease in IFT tapers off until 100% concentration. In contrast, the IFT declines linearly with increasing CH_4 concentration in the H_2–CH_4 mixture.

Local density distributions and molecular orientation analyses have elucidated the underlying mechanisms driving these IFT variations. In the H_2–CO_2–H_2O mixture, up to a 40% CO_2 concentration, there exists a consistent proportional relationship between the increased adsorption of CO_2 at the interface and its concentration in the gas mixture, resulting in a substantial reduction in IFT. Beyond this threshold, the interface becomes predominantly occupied by adsorbed CO_2, which impedes further adsorption, leading to a marginal IFT reduction with increasing CO_2 concentration. Conversely, the H_2–CH_4–H_2O mixture exhibits a constant decrease in IFT due to a steady adsorption rate of CH_4 at the interface proportional to its concentration in the gas mixture.

Furthermore, the molecular orientation of CO_2 at the interface aligns with the trends observed in IFT and adsorption behaviors. As CO_2 concentration increases from 0 to 40%, the orientational changes of CO_2 molecules contribute significantly to the reduction in IFT. Above a 40% concentration, there is little change in the molecular orientation of CO_2, correlating with the smaller IFT reduction observed. Additionally, the orientation of water molecules at the interface is influenced by the presence of adsorbed CO_2 but remains unaffected by CH_4. This differential impact on water molecule orientation by CO_2 as opposed to CH_4 is postulated as a contributing factor to the higher efficacy of CO_2 in

reducing gas-water IFT. Lastly, our study indicates that the presence of both CO_2 and CH_4 at the gas-water interface leads to a decrease in the self-diffusion of H_2 at the interface, which may be relevant for microbial dynamics in subsurface hydrogen storage facilities.

Funding

This work was supported by the New Zealand government under the MBIE contract UOCX2207 for the Endeavour research program "Pūhiko Nukutū: a green hydrogen geostorage battery in Taranaki". L. Huang acknowledges the financial support from the U.S. Department of Transportation PHMSA under Grant No. 693JK32250009CAAP.

Declaration of competing interest

The authors declare that they have no known competing financial interests or personal relationships that could have appeared to influence the work reported in this paper.

Acknowledgments

We acknowledge the OU Supercomputing Center for Education & Research (OSCER) at the University of Oklahoma, United States, and the Department of Civil and Natural Resources Engineering at the University of Canterbury, New Zealand, for computational resources and dedicated support.

Appendix A. Supplementary data

Supplementary data to this article can be found online at https://doi.org/10.1016/j.ijhydene.2024.03.341.

References

[1] Le TT, et al. Fueling the future: a comprehensive review of hydrogen energy systems and their challenges. Int J Hydrogen Energy 2023.
[2] Hassan Q, Algburi S, Sameen AZ, Salman HM, Jaszczur M. Green hydrogen: a pathway to a sustainable energy future. Int J Hydrogen Energy 2024;50:310–33.
[3] Kouchaki-Penchah H, et al. The role of hydrogen in a net-zero emission economy under alternative policy scenarios. Int J Hydrogen Energy 2024;49:173–87.
[4] Ball M, Wietschel M. The future of hydrogen–opportunities and challenges. Int J Hydrogen Energy 2009;34:615–27.
[5] Wappler M, et al. Building the green hydrogen market–Current state and outlook on green hydrogen demand and electrolyzer manufacturing. Int J Hydrogen Energy 2022;47:33551–70.
[6] Council H. Hydrogen for net zero-A critical cost-competitive energy vector. 2021.
[7] Amirthan T, Perera MSA. Underground hydrogen storage in Australia: a review on the feasibility of geological sites. Int J Hydrogen Energy 2023;48:4300–28.
[8] Bosu S, Rajamohan N. Recent advancements in hydrogen storage - comparative review on methods, operating conditions and challenges. Int J Hydrogen Energy 2024;52:352–70.
[9] Muthukumar P, et al. Review on large-scale hydrogen storage systems for better sustainability. Int J Hydrogen Energy 2023;48:33223–59.
[10] Nguyen HQ, Shabani B. Review of metal hydride hydrogen storage thermal management for use in the fuel cell systems. Int J Hydrogen Energy 2021;46:31699–726.
[11] Miocic J, et al. Underground hydrogen storage: a review. In: Geological society, London, special publications, vol. 528. SP528; 2023. p. 2022–88.
[12] Tarkowski R. Underground hydrogen storage: characteristics and prospects. Renew Sustain Energy Rev 2019;105:86–94.
[13] Jadhawar P, Saeed M. Mechanistic evaluation of the reservoir engineering performance for the underground hydrogen storage in a deep North Sea aquifer. Int J Hydrogen Energy 2024;50:558–74.
[14] Kiran R, Upadhyay R, Rajak VK, Gupta SD, Pama H. Comprehensive study of the underground hydrogen storage potential in the depleted offshore Tapti-gas field. Int J Hydrogen Energy 2023;48:12396–409.
[15] Navaid HB, Emadi H, Watson M. A comprehensive literature review on the challenges associated with underground hydrogen storage. Int J Hydrogen Energy 2023;48:10603–35.
[16] Hematpur H, Abdollahi R, Rostami S, Haghighi M, Blunt MJ. Review of underground hydrogen storage: concepts and challenges. Adv Geo-Energy Res 2023;7:111–31.
[17] Pfeiffer WT, Bauer S. Subsurface porous media hydrogen storage–scenario development and simulation. Energy Proc 2015;76:565–72.
[18] Kanaani M, Sedaee B, Asadian-Pakfar M. Role of cushion gas on underground hydrogen storage in depleted oil reservoirs. J Energy Storage 2022;45:103783.
[19] Zhao Q, Wang Y, Chen C. Numerical simulation of the impact of different cushion gases on underground hydrogen storage in aquifers based on an experimentally-benchmarked equation-of-state. Int J Hydrogen Energy 2023.
[20] Saeed M, Jadhawar P. Optimizing underground hydrogen storage in aquifers: the impact of cushion gas type. Int J Hydrogen Energy 2024;52:1537–49.
[21] Isfehani ZD, et al. Interfacial tensions of (brine+ H2+ CO2) systems at gas geo-storage conditions. J Mol Liq 2023;374:121279.
[22] Guo H, Song K, Hilfer R. SPE improved oil recovery conference. In: OnePetro; 2020.
[23] Broseta D, Tonnet N, Shah V. Are rocks still water-wet in the presence of dense CO2 or H2S? Geofluids 2012;12:280–94.
[24] Farouq Ali S, Thomas S. A realistic look at enhanced oil recovery. Sci Iran 1994;1.
[25] Delshad M, Bhuyan D, Pope G, Lake L. SPE enhanced oil recovery symposium. OnePetro; 1986.
[26] Nobakht M, Moghadam S, Gu Y. Effects of viscous and capillary forces on CO2 enhanced oil recovery under reservoir conditions. Energy Fuels 2007;21:3469–76.
[27] Slowinski Jr EJ, Gates EE, Waring CE. The effect of pressure on the surface tensions of liquids. J Phys Chem 1957;61:808–10.
[28] Massoudi R, King Jr A. Effect of pressure on the surface tension of water. Adsorption of low molecular weight gases on water at 25. deg. J Phys Chem 1974;78:2262–6.
[29] Chow YF, Maitland GC, Trusler JM. Interfacial tensions of (H2O+ H2) and (H2O+ CO2+ H2) systems at temperatures of (298–448) K and pressures up to 45 MPa. Fluid Phase Equil 2018;475:37–44.
[30] Al-Mukainah H, Al-Yaseri A, Yekeen N, Al Hamad J, Mahmoud M. Wettability of shale–brine–H2 system and H2-brine interfacial tension for assessment of the sealing capacities of shale formations during underground hydrogen storage. Energy Rep 2022;8:8830–43.
[31] Hosseini M, Fahimpour J, Ali M, Keshavarz A, Iglauer S. H2– brine interfacial tension as a function of salinity, temperature, and pressure; implications for hydrogen geo-storage. J Petrol Sci Eng 2022;213:110441.
[32] Fukuzawa K, Watanabe K, Yasuda K, Ohmura R. Interfacial tension measurements in the (CO2+ H2) gas mixture and water system at temperatures from 271.2 K to 280.2 K and pressures up to 7.0 MPa. J Chem Therm 2018;119:20–5.
[33] Doan QT, Keshavarz A, Miranda CR, Behrenbruch P, Iglauer S. Molecular dynamics simulation of interfacial tension of the CO2-CH4-water and H2-CH4-water systems at the temperature of 300 K and 323 K and pressure up to 70 MPa. J Energy Storage 2023;66:107470.
[34] Mirchi V, Dejam M, Alvarado V. Interfacial tension and contact angle measurements for hydrogen-methane mixtures/brine/oil-wet rocks at reservoir conditions. Int J Hydrogen Energy 2022;47:34963–75.
[35] Doan QT, Keshavarz A, Miranda CR, Behrenbruch P, Iglauer S. A prediction of interfacial tension by using molecular dynamics simulation: a study on effects of cushion gas (CO2, N2 and CH4) for Underground Hydrogen Storage. Int J Hydrogen Energy 2024;50:1607–15.
[36] Vasseghian Y, Bahadori A, Khataee A, Dragoi E-N, Moradi M. Modeling the interfacial tension of water-based binary and ternary systems at high pressures using a neuro-evolutive technique. ACS Omega 2019;5:781–90.
[37] Yan W, Zhao G-Y, Chen G-J, Guo T-M. Interfacial tension of (methane+ nitrogen)+ water and (carbon dioxide+ nitrogen)+ water systems. J Chem Eng Data 2001;46:1544–8.
[38] Zhang R-h, et al. Numerical simulation and laboratory experiments of CO2 sequestration and being as cushion gas in underground natural gas storage reservoirs. J Nat Gas Sci Eng 2021;85:103714.
[39] Middleton RS, et al. The cross-scale science of CO 2 capture and storage: from pore scale to regional scale. Energy Environ Sci 2012;5:7328–45.
[40] Bennion B, Bachu S. SPE/DOE symposium on improved oil recovery. OnePetro; 2006.
[41] Cho J, Kim TH, Chang N, Lee KS. Effects of relative permeability change resulting from interfacial tension reduction on vertical sweep efficiency during the CO2-LPG hybrid EOR process. Energy Sources, Part A Recovery, Util Environ Eff 2018;40:1242–9.
[42] Zivar D, Kumar S, Foroozesh J. Underground hydrogen storage: a comprehensive review. Int J Hydrogen Energy 2021;46:23436–62.
[43] Hassanpouryouzband A, Joonaki E, Edlmann K, Heinemann N, Yang J. Thermodynamic and transport properties of hydrogen containing streams. Sci Data 2020;7:222.
[44] Chang Q, Huang L, Wu X. A molecular dynamics study on low-pressure carbon dioxide in the water/oil interface for enhanced oil recovery. SPE J 2023;28:643–52.
[45] Liu B, et al. Reduction in interfacial tension of water–oil interface by supercritical CO2 in enhanced oil recovery processes studied with molecular dynamics simulation. J Supercrit Fluids 2016;111:171–8.
[46] Toutouni R, Kubelka J, Piri M. Liquid–vapor interfacial tension in alkane mixtures: improving predictive capabilities of molecular dynamics simulations. J Phys Chem B 2022;126:1136–46.
[47] Xu J, et al. Effect of surfactant headgroups on the oil/water interface: an interfacial tension measurement and simulation study. J Mol Struct 2013;1052:50–6.
[48] Zhao J, Yao G, Ramisetti SB, Hammond RB, Wen D. Molecular dynamics simulation of the salinity effect on the n-decane/water/vapor interfacial equilibrium. Energy Fuels 2018;32:11080–92.
[49] Guo Z, Zhang X. Enhanced fluctuation for pinned surface nanobubbles. Phys Rev 2019;100:052803.
[50] Liu Y, Lafitte T, Panagiotopoulos AZ, Debenedetti PG. Simulations of vapor–liquid phase equilibrium and interfacial tension in the CO2–H2O–NaCl system. AIChE J 2013;59:3514–22.

[51] Novak BR, Maginn EJ, McCready MJ. Comparison of heterogeneous and homogeneous bubble nucleation using molecular simulations. Phys Rev B 2007;75:085413.
[52] Harris JG, Yung KH. Carbon dioxide's liquid-vapor coexistence curve and critical properties as predicted by a simple molecular model. J Phys Chem 1995;99:12021–4.
[53] Zhong H, et al. Molecular dynamics simulation of transport and structural properties of CO2 using different molecular models. J Chem Eng Data 2015;60:2188–96.
[54] Mark P, Nilsson L. Structure and dynamics of the TIP3P, SPC, and SPC/E water models at 298 K. J Phys Chem 2001;105:9954–60.
[55] Chen C, Hu W, Li W, Song Y. Model comparison of the CH4/CO2/water system in predicting dynamic and interfacial properties. J Chem Eng Data 2019;64:2464–74.
[56] Martin MG, Siepmann JI. Transferable potentials for phase equilibria. 1. United-atom description of n-alkanes. J Phys Chem B 1998;102:2569–77.
[57] Köster A, Thol M, Vrabec J. Molecular models for the hydrogen age: hydrogen, nitrogen, oxygen, argon, and water. J Chem Eng Data 2018;63:305–20.
[58] van Rooijen W, et al. Interfacial tensions, solubilities, and transport properties of the H2/H2O/NaCl system: a molecular simulation study. J Chem Eng Data 2023.
[59] Yang Y, Narayanan Nair AK, Sun S. Molecular dynamics simulation study of carbon dioxide, methane, and their mixture in the presence of brine. J Phys Chem B 2017;121:9688–98.
[60] de Lara LS, Michelon MF, Miranda CR. Molecular dynamics studies of fluid/oil interfaces for improved oil recovery processes. J Phys Chem B 2012;116:14667–76.
[61] Li X, Ross DA, Trusler JM, Maitland GC, Boek ES. Molecular dynamics simulations of CO2 and brine interfacial tension at high temperatures and pressures. J Phys Chem B 2013;117:5647–52.
[62] Vega C, de Miguel E. Surface tension of the most popular models of water by using the test-area simulation method. J Chem Phys 2007;126:154707.
[63] Chen F, Smith PE. Simulated surface tensions of common water models. J Chem Phys 2007;126:221101.
[64] Rahbari A, et al. Solubility of water in hydrogen at high pressures: a molecular simulation study. J Chem Eng Data 2019;64:4103–15.
[65] Zhang Y, Feller SE, Brooks BR, Pastor RW. Computer simulation of liquid/liquid interfaces. I. Theory and application to octane/water. J Chem Phys 1995;103:10252–66.
[66] Mirzaeifard S, Servio P, Rey AD. Molecular dynamics characterization of temperature and pressure effects on the water-methane interface. Colloid Interf Sci Commun 2018;24:75–81.
[67] Jerauld GR, Kazemi A. An improved simple correlation for accurate estimation of CO2-Brine interfacial tension at reservoir conditions. J Petrol Sci Eng 2022;208:109537.
[68] Dong F, Zhou J, Xu S, Chen X, Zhang P. Prediction model of interfacial tension of H2/H2O and (N2+ H2)/H2O systems using the linear gradient theory in combination with PR-EOS. J Mol Liq 2024;395:123809.
[69] Ren Q-Y, Chen G-J, Yan W, Guo T-M. Interfacial tension of (CO2+ CH4)+ water from 298 K to 373 K and pressures up to 30 MPa. J Chem Eng Data 2000;45:610–2.
[70] Kashefi K, Pereira LM, Chapoy A, Burgass R, Tohidi B. Measurement and modelling of interfacial tension in methane/water and methane/brine systems at reservoir conditions. Fluid Phase Equil 2016;409:301–11.
[71] Georgiadis A, Maitland G, Trusler JM, Bismarck A. Interfacial tension measurements of the (H2O+ CO2) system at elevated pressures and temperatures. J Chem Eng Data 2010;55:4168–75.
[72] Bachu S, Bennion DB. Interfacial tension between CO2, freshwater, and brine in the range of pressure from (2 to 27) MPa, temperature from (20 to 125) C, and water salinity from (0 to 334 000) mg· L− 1. J Chem Eng Data 2009;54:765–75.
[73] Guo Q, et al. Molecular dynamics simulation of the interfacial properties of methane-water and methane-brine systems. Mol Simulat 2023;49:1215–28.
[74] Miqueu C, Miguez JM, Pineiro MM, Lafitte T, Mendiboure B. Simultaneous application of the gradient theory and Monte Carlo molecular simulation for the investigation of methane/water interfacial properties. J Phys Chem B 2011;115:9618–25.
[75] Li W, Jin Z. Molecular dynamics simulations of natural gas-water interfacial tensions over wide range of pressures. Fuel 2019;236:480–92.
[76] Prasad SK, Sangwai JS, Byun H-S. A review of the supercritical CO2 fluid applications for improved oil and gas production and associated carbon storage. J CO2 Util 2023;72:102479.
[77] Shiga M, Morishita T, Sorai M. Interfacial tension of carbon dioxide-water under conditions of CO2 geological storage and enhanced geothermal systems: a molecular dynamics study on the effect of temperature. Fuel 2023;337:127219.
[78] Minkara MS, et al. Monte Carlo simulations probing the liquid/vapour interface of water/hexane mixtures: adsorption thermodynamics, hydrophobic effect, and structural analysis. Mol Phys 2018;116:3283–91.
[79] Naeiji P, Woo TK, Alavi S, Ohmura R. Molecular dynamics simulations of interfacial properties of the CO2–water and CO2–CH4–water systems. J Chem Phys 2020;153.
[80] Zhao L, Tao L, Lin S. Molecular dynamics characterizations of the supercritical CO2–mediated hexane–brine interface. Ind Eng Chem Res 2015;54:2489–96.
[81] Ebigbo A, Golfier F, Quintard M. A coupled, pore-scale model for methanogenic microbial activity in underground hydrogen storage. Adv Water Resour 2013;61:74–85.
[82] Yuan L, Zhao C, Xu Y, Zhang Y. Molecular dynamics simulation of CO2 diffusion in a carbonated water–decane system. Energies 2020;13:6031.
[83] Chang Q, et al. An atomistic model of aged asphalt guided by the oxidation chemistry of benzylic carbon with application to asphalt rejuvenated with a triglyceride. Construct Build Mater 2023;400:132743.
[84] Chang Q, Huang L, Wu Y. Evaluating the influence of waste cooking oil molecular structure on aged asphalt modification. Construct Mater 2023;3:543–57.
[85] Deng X, Zhang Q, Zhang Z, Li Q, Liu X. Adsorption and diffusion behavior of CO2/H2 mixture in calcite slit pores: a molecular simulation study. J Mol Liq 2022;346:118306.
[86] Groß T, Buchhauser J, Lüdemann H-D. Self-diffusion in fluid carbon dioxide at high pressures. J Chem Phys 1998;109:4518–22.
[87] Dawson R, Khoury F, Kobayashi R. Self-diffusion measurements in methane by pulsed nuclear magnetic resonance. AIChE J 1970;16:725–9.
[88] Cadogan SP, Maitland GC, Trusler JM. Diffusion coefficients of CO2 and N2 in water at temperatures between 298.15 K and 423.15 K at pressures up to 45 MPa. J Chem Eng Data 2014;59:519–25.
[89] Pereira LM, et al. Study of the impact of high temperatures and pressures on the equilibrium densities and interfacial tension of the carbon dioxide/water system. J Chem Therm 2016;93:404–15.
[90] Liu Y, Li HA, Okuno R. Measurements and modeling of interfacial tension for CO2/CH4/brine systems under reservoir conditions. Ind Eng Chem Res 2016;55:12358–75.